ADVANCED MATERIALS

Supporting Information

Direct Observations of Nanofilament Evolution in Switching Processes in HfO$_2$-Based Resistive Random Access Memory by In Situ TEM Studies

Chao Li, Bin Gao, Yuan Yao, Xiangxiang Guan, Xi Shen, Yanguo Wang, Peng Huang, Lifeng Liu, Xiaoyan Liu, Junjie Li, Changzhi Gu, Jinfeng Kang,* and Richeng Yu*

Direct Observations of Nano-filament Evolution in Switching Processes in HfO₂-based Resistive Random Access Memory by *in situ* TEM studies

Chao Li[1,†], Bin Gao[2,†], Yuan Yao[1,†], Xiangxiang Guan[1,3], Xi Shen[1], Yanguo Wang[1], Peng Huang[2], Lifeng Liu[2], Xiaoyan Liu[2], Junjie Li[1], Changzhi Gu[1], Jinfeng Kang[2,], Richeng Yu[1,3,*]*

1. Beijing National Laboratory of Condensed Matter Physics, Institute of Physics, Chinese Academy of Sciences, Beijing 100190, People's Republic of China

2. Institute of Microelectronics, Peking University, Beijing 100871, People's Republic of China

3. School of Physical Sciences, University of Chinese Academy of Sciences, Beijing 100049, People's Republic of China

§: These authors have same contributions.

*: Corresponding authors: rcyu@aphy.iphy.ac.cn; kangjf@pku.edu.cn
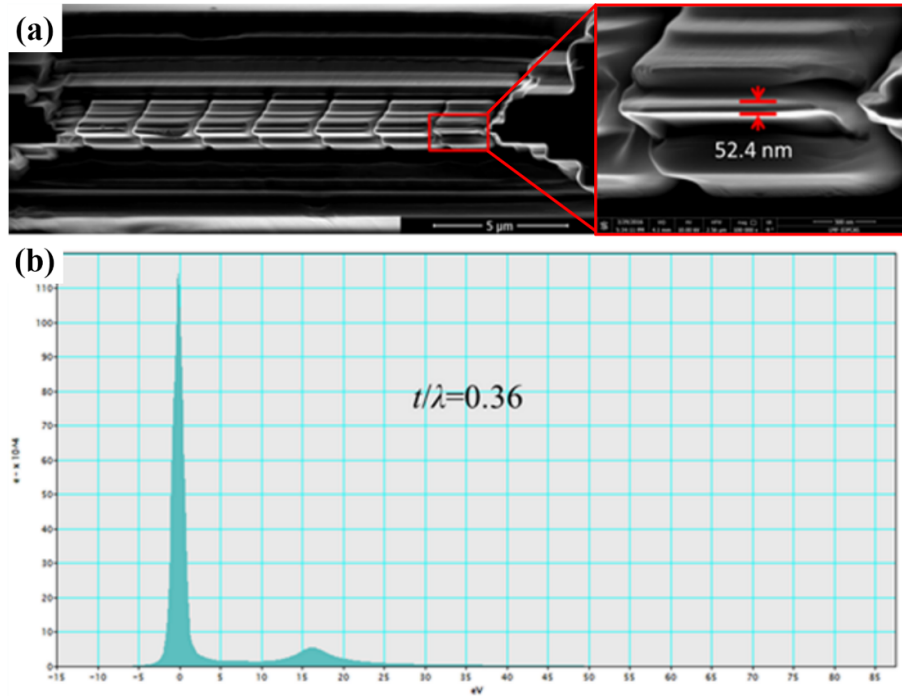
Supplementary Information

1. *In situ* **I-V tests**
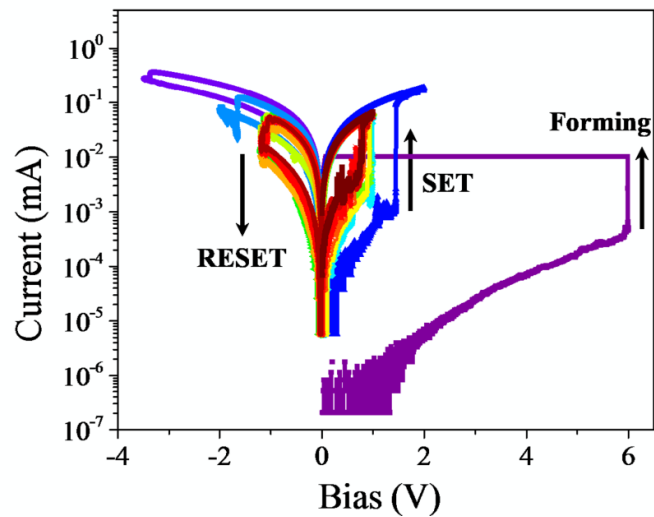
Fig. S1. Repeated cycling test for a sample with a thickness of about 100 nm.

The repeatable I-V test is measured for a thicker TEM sample since the thinner one is easy to damage under several cycles. The thicker sample has smaller forming, SET and RESET voltages than the thinner one.

2. Thickness determination

Fig. S2. (a) SEM image of the FIB prepared sample for TEM *in situ* tests. The thickness of the samples is about 50 nm, and (b) the low loss energy spectrum of the silicon beneath the HfO_x layer with the same thickness as the silicon layer indicating that the relative thickness t/λ is 0.36.

The thickness of the sample for electron holography and EELS characterizations could be measured in SEM image directly (Fig. S2(a)). Another method is to use EELS plasmon peak for estimating the relative thickness t/λ, where λ is the mean free path of electron in the sample (Fig. S2(b)). If $\lambda = 150$ nm[1], the thickness is 54 nm, which is consistent with the SEM measurement.

3. Holography experiments
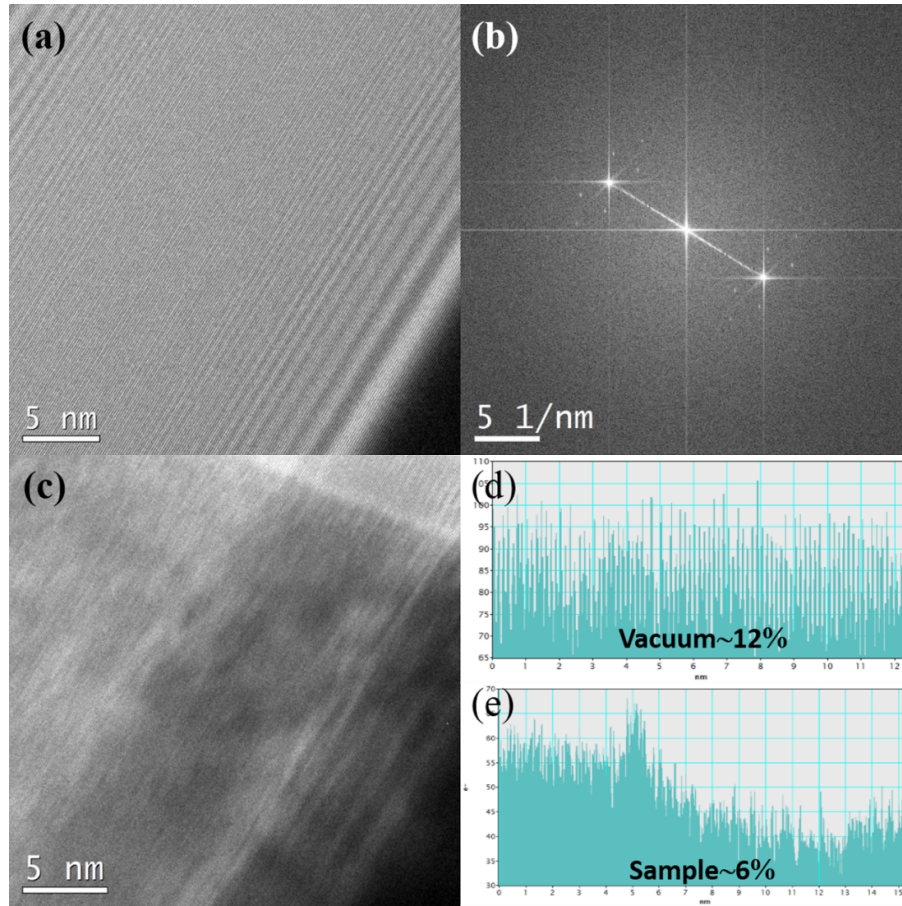
Fig. S3. (a) Reference hologram, (b) the FFT of the reference hologram where the corresponding resolution of 0.43 nm for sideband can be readily discerned, (c) the hologram of the dielectric layer, (d) the reference hologram, and (e) the sample hologram.

The contrast of the interference fringes in the sample hologram is degraded from 12 to 6% due to the deterioration of the beam coherence as shown in Figs. S3(d) and S3(e). Therefore, many extracted phase images are averaged to improve the S/N ratio.

4. Phase retrieving
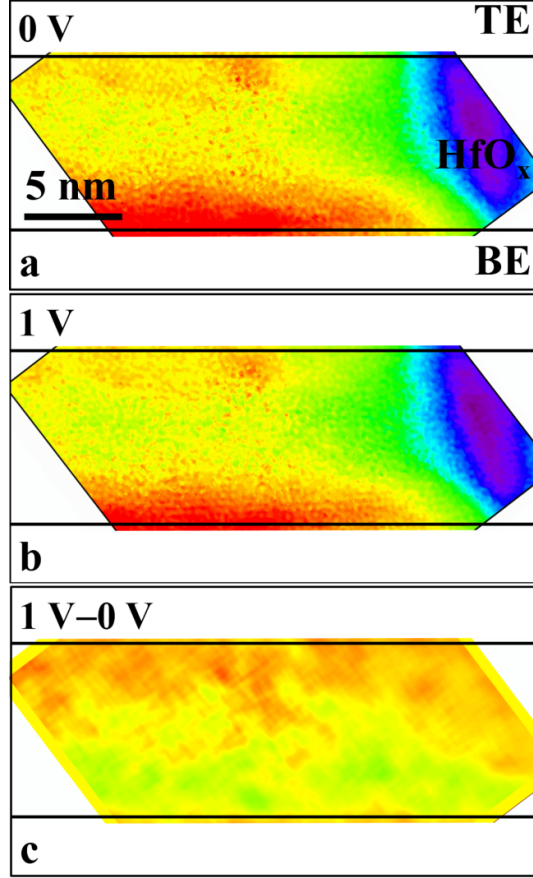
Fig. S4. Reconstructed phase images of (a) zero bias, (b) 1 V, (c) $\Delta\varphi^{1V}(x, y)$ calculated from panels (a) and (b) by Eq. (3).

The image processing to extract the bias-induced phase map $\Delta\varphi^{bias}(x, y)$ is shown here. If no bias is applied, the phase distribution $\varphi^{0V}(x, y)$ of the sample is determined by the phase difference between the objective wave and the reference vacuum wave which can be regarded as zero.

$$\varphi^{0V}(x, y) = \varphi_{obj}^{iner}(x, y) + \varphi_{obj}^{dyn}(x, y), \qquad (1)$$

where $\varphi_{obj}^{iner}(x, y)$ and $\varphi_{obj}^{dyn}(x, y)$ are the inner potential phase and dynamic disturbance, respectively; $\varphi^{0V}(x, y)$ describes the intrinsic physical properties of the sample and does not vary with bias. When a bias is applied, $\varphi^{bias}(x, y)$ is

$$\varphi^{bias}(x, y) = \varphi_{obj}^{iner}(x, y) + \varphi_{obj}^{dyn}(x, y) + \varphi_{obj}^{bias}(x, y), \qquad (2)$$

where $\varphi_{obj}^{bias}(x,y)$ is the phase shift caused by the bias-induced charges. Subtracting $\varphi^{0V}(x,y)$ from $\varphi^{bias}(x,y)$ yields the difference $\Delta\varphi^{bias}(x,y)$ expressed as

$$\Delta\varphi^{bias}(x,y) = \varphi^{bias}(x,y) - \varphi^{0V}(x,y) = \varphi_{obj}^{bias}(x,y). \tag{3}$$

Furthermore, $\Delta\varphi^{bias}(x,y)$ can be presented as

$$\Delta\varphi^{bias}(x,y) = \varphi_{obj}^{bias}(x,y) = C_E V_{pro}^{bias}(x,y)t \ , \tag{4}$$

where C_E is 0.0073/(V nm) for 200 kV electrons, $V_{pro}^{bias}(x,y)$ is the 'projected' (along electron beam direction) potential induced by generated charges in dielectric layers, and t is the sample thickness. Therefore, the charge distribution can be deduced from the $V_{pro}^{bias}(x,y)$ maps.

Because the conductive TiN could be regarded as an equipotential electrode whose potential should be constant, the standard deviation (SD) of the retrieved phase in this part is a reasonable estimation for the phase error. Table S1 lists the SDs at different biases. The error is less than 0.2 radian.

Table S1. Standard deviations of retrieved phase in TiN layer at different biases.

| Bias (V)	1	2	3	4	5	6	7
SD (rad)	0.11	0.16	0.15	0.14	0.17	0.13	0.17
Bias (V)	-1	-2	-3	-4	-5	-6	-6.5
SD (rad)	0.15	0.18	0.18	0.17	0.17	0.19	0.16

5. EELS mapping
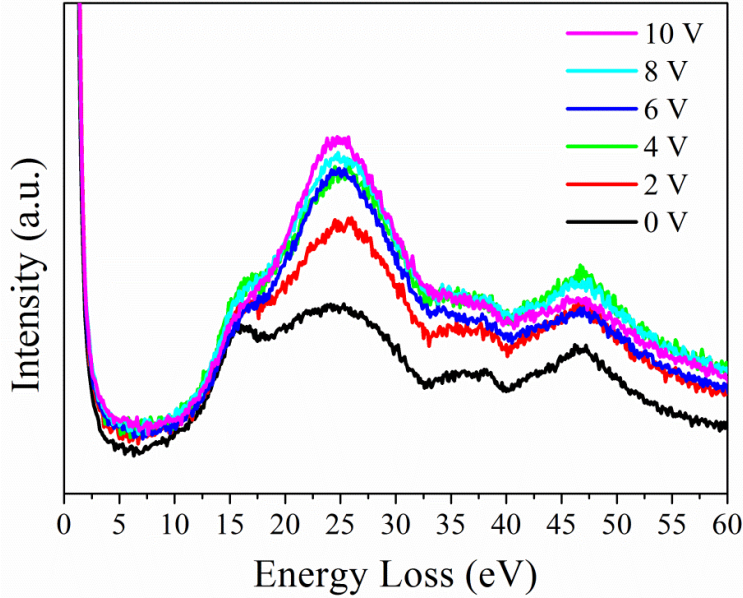
Fig. S5. Variations of plasmon peaks of the HfO$_x$ layer with energy loss under different biases. The feature around 26 eV is changed obviously by the bias.

Generally, there are five peaks at 16.4 eV, 26 eV, 35 eV, 37 eV and 46.4 eV in the low energy loss spectrum of HfO$_x$ film (Fig. S5). The theoretical calculation indicates that the peak at 16.4 eV corresponds to the valence plasmon vibration and the peak at 26 eV is related to excitations from O 2s to Hf 5d.[2-4] It has been reported that these peaks are sensitive to the oxygen concentration in the hafnia film, especially for the 26 eV peak whose intensity can increase compared with others in low oxygen content HfO$_2$ sample. [5, 6] So the height change of 26 eV peak is an indicator to characterize the oxygen consumption in the hafnia layer in the *in situ* experiment: the increase of oxygen consumption implies the dissipation of the oxygen or the generations of oxygen vacancies, and vice versa. The low-loss energy-filtered images at this peak are acquired to map the spatial variations of the oxygen in hafnia film under different biases, while the energy loss center is situated at 24 eV and the width of the energy window is 4 eV that can isolate the 26 eV peak effectively.

6. Physical model of resistive switching in metal-oxides
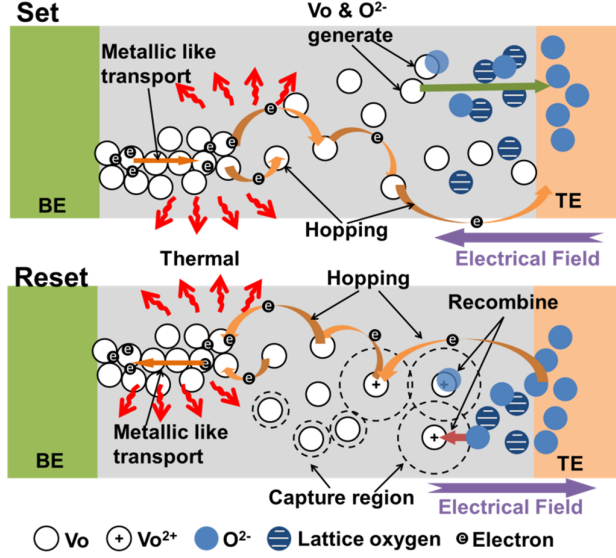
Fig. S6. Schematic physical process of resistive switching used in the model.

In the Set/Forming process, the generations of oxygen vacancies and the migration of dissociated oxygen ion (O^{2-}) to top electrode lead to the formation of conductive filament (CF) connecting anode and cathode, which results in the switching of device from high resistance state to low resistance state. In the RESET process, the dissociated O^{2-} ions are released from the top electrode and then migrate to the nearby oxygen vacancies (V_O's) and recombine with them, which causes the CF to be ruptured and the RRAM to be switched from the LRS to the HRS. Therefore, the main microscopic processes during switching are summarized as follows: generating V_O, migrating O^{2-} ions, recombining O^{2-} ions with electron-depleted V_O, and absorbing and releasing O^{2-} ions by electrode. The generation probability (P_g) of V_O under electric field during dt is governed by the following equation:

$$P_g(E,T,dt) = fdt \exp(-\frac{E_a - \alpha_a ZeE}{k_B T}) \quad , \tag{5}$$

where E is the electric field, T is the local temperature, f is the vibration frequency of oxygen atom, E_a is the average active energy of V_O, α_a is the enhancement factor of

the electric field for lowering E_a, Z is the charge number of oxygen ion (here $Z=2$), e is the unit charge, and k_B is the Boltzmann constant. The hopping probability (P_h) of the dissociated O^{2-} in the oxide layer under the electric field during dt can be described as

$$P_h(E,T,dt) = fdt \exp(-\frac{E_h - \alpha_h Z e E}{k_B T}), \qquad (6)$$

where E_h is the hopping barrier of O^{2-} and α_h is the enhancement factor of the electric field for lowering E_h. The recombination between O^{2-} and electron-depleted V_O is modeled as an energy relaxation process and governed by the following equation:

$$P_r(T,dt) = fdt \exp(-\frac{\Delta E_r}{k_B T}), \qquad (7)$$

where P_r (T, dt) is the probability of the recombination between V_O and O^{2-} during dt, ΔE_r is the relaxation energy in the recombination process. The top electrode is the active electrode and acts as an O^{2-} reservoir that can release O^{2-} with the probability (P_m) governed by the equation:

$$P_m(V,T,dt) = fdt \exp(-\frac{E_i - \gamma Z e V}{k_B T}), \qquad (8)$$

where $P_m(V,T,dt)$ is the probability of electrode released O^{2-} during dt, V is the external voltage, E_i is the energy barrier between the electrode and oxide, γ is the enhancement factor of the external voltage in the O^{2-} release process.

7. Monte Carlo simulation of the resistive switching process in metal oxide
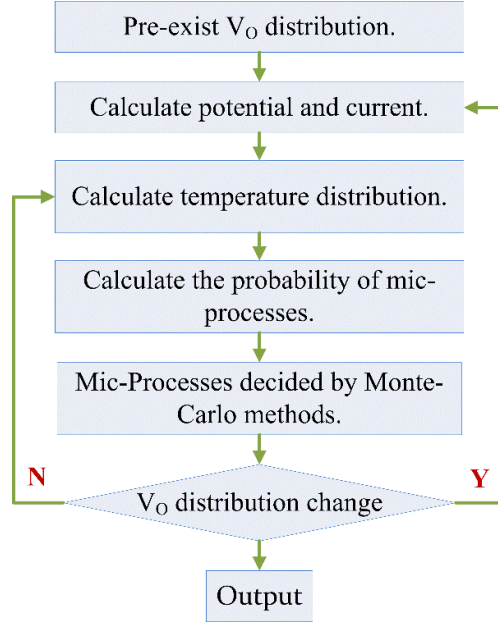
Fig. S7. Simulation algorithm flow.

In order to simulate the above mentioned microscopic processes self-consistently and efficiently, a resistor network based on the percolation theory is introduced. The potential and current can be solved by the Kirchhoff law and the local temperature can be obtained from the Fourier heat-flow equation:

$$C\frac{\partial T}{\partial t}=\nabla(k\cdot\nabla T)+Q\,,\tag{9}$$

where C is the specific heat per unit volume of the metal oxide, k is the thermal conductivity of the metal oxide, and Q is the Joule heat power density. Each physical quantity is updated after each microscopic physical process based on Eqs. $(5)-(9)$. Then the microscopic process can be simulated self-consistently. Fig. S7 shows the simulation flowcharts. The device mesh in our simulation is h×h, where h is the distance between two oxygen sites, which ensures that one oxygen site is located in one mesh. The size of the simulated device is 10nm×40nm. The sites of the pre-existing V_O's are random, and determined by the Monte-Carlo method. The

percentage of the pre-existing V_O's can vary from zero to unit for different devices in the simulation. The probabilities of generation of V_O and migration of oxygen ion can be given respectively by Eqs. (5) and (6) based on the distribution of potential and the located temperature. Here the current, potential and local temperature are self-consistently solved, reflecting that the oxygen vacancy distribution affects the calculations of those values. Switching on the device and ending the simulation are determined by the actual need.

8. Simulated oxygen vacancy distribution

According to the physical model and Monte-Carlo method, we simulate the distribution of V_O's in the forming process as shown in Fig. S8. The top and bottom electrodes are the anode and cathode, respectively, in the forming process. The pink dots represent Vo's in the oxide layer. At first, V_O's are distributed randomly in the oxide layer (Fig. S8(a)). When voltage is applied, V_O clusters emerge (Figs. S8(b) − S8(f)). The V_O filament begins to form in the oxide layer and extends to the top and bottom electrodes. Finally, the V_O filament connects the two electrodes, and thus the forming process is completed (Fig. S8(g)). The evolution of V_O distribution in the simulation is consistent with the variation trends as shown in Figs. 3 and 5 of the main text.
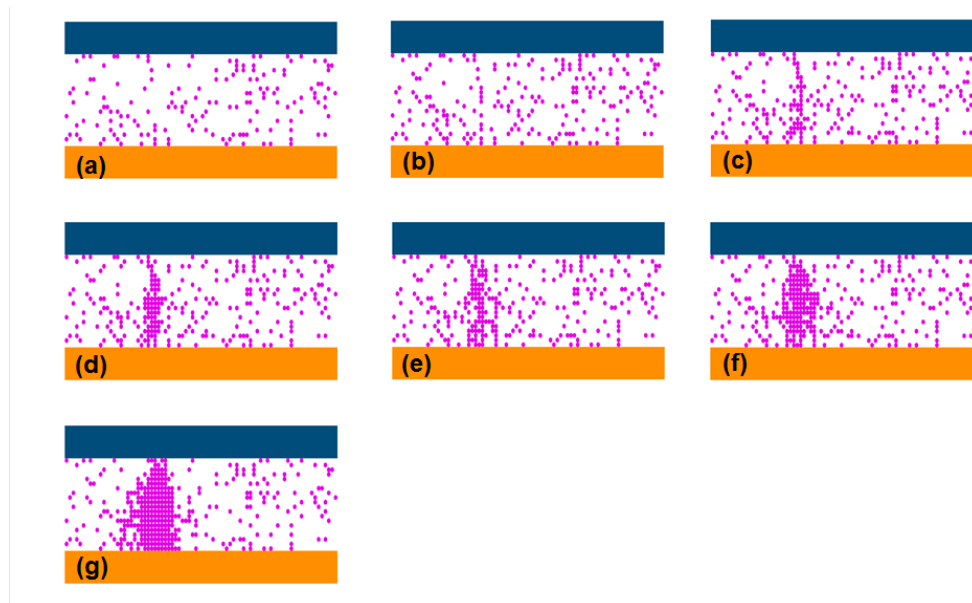
Fig. S8. Simulated V_O distributions in the forming process.

Fig. S9 shows the V_O distributions in the reset process. The filament shrinks from the top electrode (cathode) interface, and finally a gap region forms. This process is also consistent with the variation trend as shown in Fig. 4 of the main text.
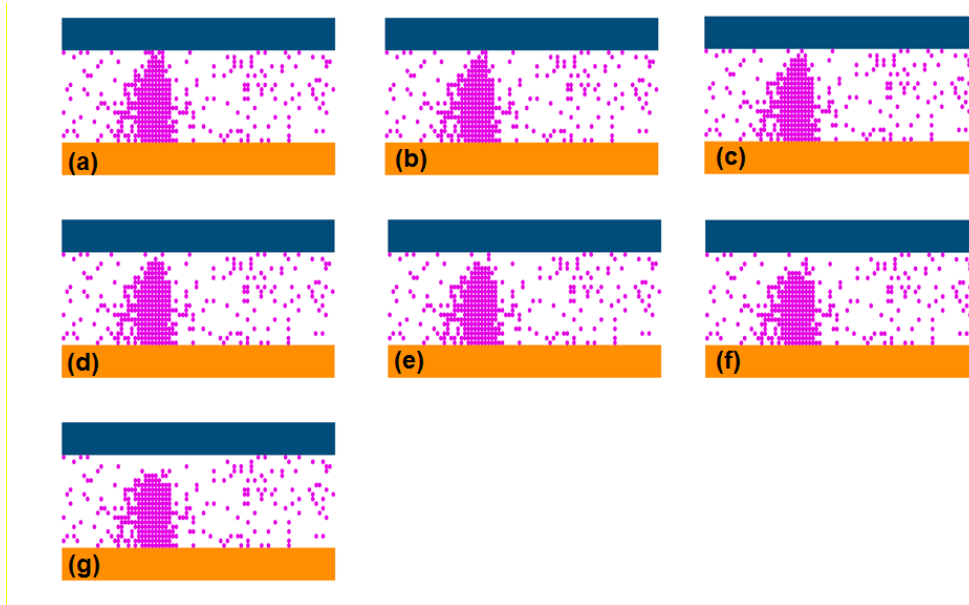
Fig. S9. Simulated Vo distributions in the reset process.

It should be noticed that the simulated V_O distribution cannot exactly match the experimental results since grain boundary and amorphous effects are not taken into consideration in the simulation. However, the evolution trends in the forming and resistive switching processes still reflect that the V_O generation and recovery are responsible for the formation and rupture of CF and the electron path through the oxide layer.
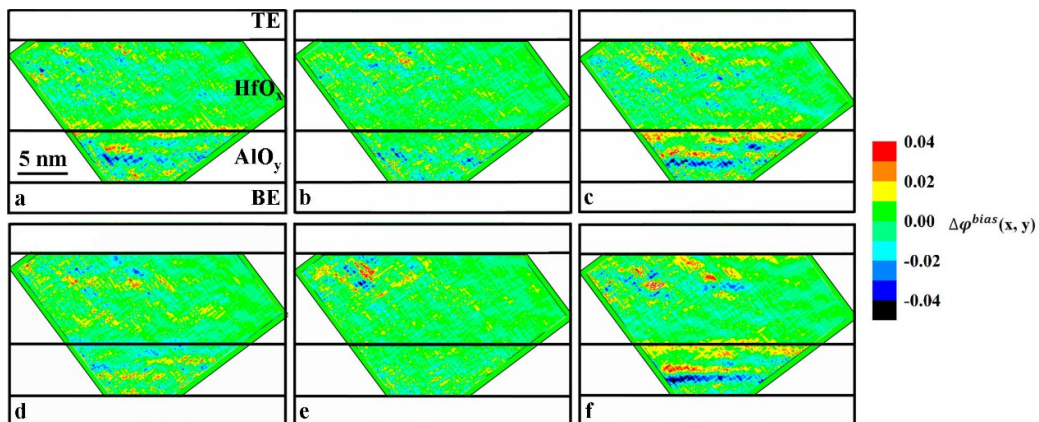
9. Differential phase images from two consecutive tests.

Fig. S10 and S11 show the differential phase images from two consecutive tests in the forming and reset processes, respectively. The contrast only displays the negative

charge increasing near the HfO$_x$ top surface in the forming process, but the negative charge decreasing fast near the HfO$_x$ top surface in the reset process. These details of the whole view field can be destroyed by the noise. The breaks of the CFs cannot be distinguished because no real charge signs but relative charge changes appear in the differential images.
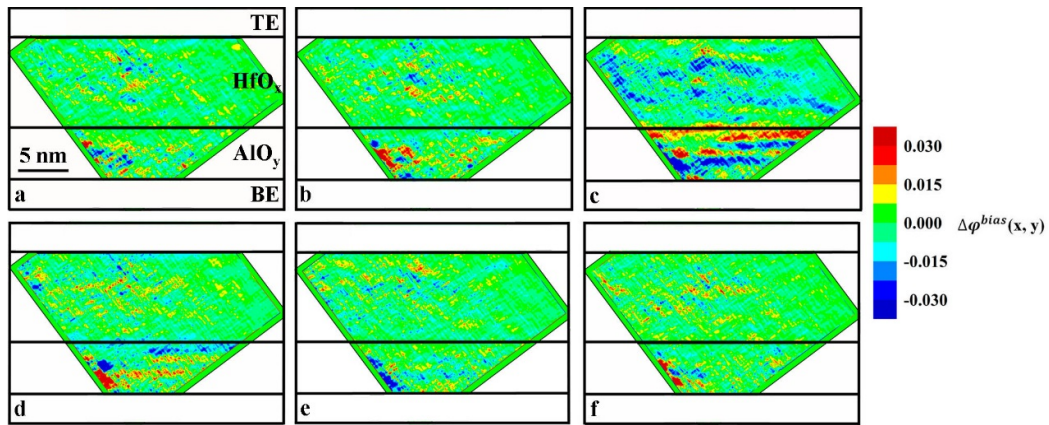

Fig. S10. Phase images treated by differentiating the results from two consecutive tests in the forming process. Panels (a) − (f) show the differential phase images of 2V-1V, 3V-2V, 4V-3V, 5V-4V, 6V-5V and 7V-6V, respectively.

Fig. S11. Phase images treated by differentiating the results from two consecutive tests during forming process. Panels (a) – (f) are the differential phase images of -2V-(-1V), -3V-(-2V), -4V-(-3V), -5V-(-4V), -6V-(-5V) and -6.5V-(-6V), respectively.

10. I-V curve in the forming process.
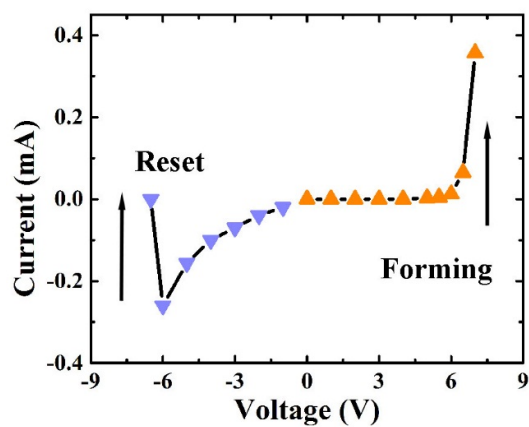
Fig. S12. I–V curve measured during acquiring the holography images.

References of Supplementary Information

[1] Potapov, P. L. The experimental electron mean-free-path in Si under typical (S)TEM conditions. *Ultramicroscopy*, **14,** 721–24 (2014).

[2] Guedj, C.; Hung, L.; Zobelli, A.; Blaise, P.; Sottile, F.; Olevano, V. Evidence for anisotropic dielectric properties of monoclinic hafnia using valence electron energy-loss spectroscopy in high-resolution transmission electron microscopy and ab initio time-dependent density-functional theory. Appl. Phys. Lett. 2014, 105, 222904.

[3] Park, J.; Yang, M. Determination of complex dielectric functions at HfO2/Si interface by using STEM-VEELS. Micron, 2009, 40, 365-369.

[4] Kang, Y. S.; Kim, D. K.; Kang, H. K.; Cho, S.; Choi, S.; Kim, H.; Seo, J. H.; Lee, J.; Cho, M. H. Defect states below the conduction band edge of HfO_2 grown on InP by atomic layer deposition, J. Phys. Chem. C 2015, 119, 6001-6008.

[5] Jang, J. H.; Hwang, C. S.; Jung, H. S.; Kim, M.; Kim, J. H.; Lee, S. Y. Investigation of oxygen-related defects and the electrical properties of atomic layer deposited HfO2 films using electron energy-loss spectroscopy. J. Appl. Phys. 2011, 109, 023718.

[6] Li, C. *et al.* Dynamic observation of oxygen vacancies in hafnia layer by in situ transmission electron microscopy. *Nano Research* **8**, 3571 (2015).

[7] Gao, B. *et al*. Oxide-Based RRAM: Unified Microscopic Principle for both Unipolar and Bipolar Switching, Tech. Dig. IEDM., 417 (2011).

[8] Huang, P. *et al*. Optimization of conductive filament of oxide-based resistive-switching random access memory for low operation current by stochastic simulation. *Jpn. J. Appl. Phys.* **52**, 04CD04 (2013).